Permanent WRAP URL:
http://wrap.warwick.ac.uk/78555

A note on versions:
The version presented in WRAP is the published version or, version of record, and may be cited as it appears here.

For more information, please contact the WRAP Team at: wrap@warwick.ac.uk

warwick.ac.uk/lib-publications

Photodynamical mass determination of the multiplanetary system K2-19

S. C. C. Barros,[1,2]★ J. M. Almenara,[3,4] O. Demangeon,[1] M. Tsantaki,[2] A. Santerne,[2]
D. J. Armstrong,[5] D. Barrado,[6] D. Brown,[5] M. Deleuil,[1] J. Lillo-Box,[6] H. Osborn,[5]
D. Pollacco,[5] L. Abe,[7] P. Andre,[8] P. Bendjoya,[7] I. Boisse,[1] A. S. Bonomo,[9] F. Bouchy,[1]
G. Bruno,[1] J. Rey Cerda,[10] B. Courcol,[1] R. F. Díaz,[10] G. Hébrard,[11,12] J. Kirk,[5]
J. C. Lachurié,[8] K. W. F. Lam,[5] P. Martinez,[8] J. McCormac,[5] C. Moutou,[1,13]
A. Rajpurohit,[1] J.-P. Rivet,[7] J. Spake,[5] O. Suarez,[7] D. Toublanc[8,14] and S. R. Walker[5]

[1]*Aix Marseille Université, CNRS, LAM (Laboratoire d'Astrophysique de Marseille) UMR 7326, F-13388 Marseille, France*
[2]*Instituto de Astrofísica e Ciências do Espaço, Universidade do Porto, CAUP, Rua das Estrelas, PT4150-762 Porto, Portugal*
[3]*Univ. Grenoble Alpes, IPAG, F-38000 Grenoble, France*
[4]*CNRS, IPAG, F-38000 Grenoble, France*
[5]*Department of Physics, University of Warwick, Gibbet Hill Road, Coventry CV4 7AL, UK*
[6]*Departamento de Astrofísica, Centro de Astrobiología (CSIC-INTA), ESAC campus, E-28691 Villanueva de la Cañada (Madrid), Spain*
[7]*Laboratoire Lagrange, UMR7239, Université de Nice Sophia-Antipolis, CNRS, Observatoire de la Cote d'Azur, F-06300 Nice, France*
[8]*Observatoire de Belesta en Lauragais - Assoc. Astronomie Adagio 30 Route de Revel, F-31450 Varennes, France*
[9]*INAF - Osservatorio Astrofisico di Torino, via Osservatorio 20, I-10025 Pino Torinese, Italy*
[10]*Observatoire Astronomique de l'Universite de Genève, 51 chemin des Maillettes, CH-1290 Versoix, Switzerland*
[11]*Institut d'Astrophysique de Paris, UMR7095 CNRS, Université Pierre & Marie Curie, 98bis boulevard Arago, F-75014 Paris, France*
[12]*Observatoire de Haute-Provence, Université d'Aix-Marseille & CNRS, F-04870 Saint Michel l'Observatoire, France*
[13]*CNRS, Canada–France–Hawaii Telescope Corporation, 65-1238 Mamalahoa Hwy., Kamuela, HI 96743, USA*
[14]*Universite de Toulouse, UPS-CNRS, IRAP, 9 Av. colonel Roche, F-31028 Toulouse cedex 4, France*

ABSTRACT

K2-19 is the second multiplanetary system discovered with K2 observations. The system is composed of two Neptune size planets close to the 3:2 mean-motion resonance. To better characterize the system we obtained two additional transit observations of K2-19b and five additional radial velocity observations. These were combined with K2 data and fitted simultaneously with the system dynamics (photodynamical model) which increases the precision of the transit time measurements. The higher transit time precision allows us to detect the chopping signal of the dynamic interaction of the planets that in turn permits to uniquely characterize the system. Although the reflex motion of the star was not detected, dynamic modelling of the system allowed us to derive planetary masses of $M_b = 44 \pm 12$ M$_\oplus$ and $M_c = 15.9 \pm 7.0$ M$_\oplus$ for the inner and the outer planets, respectively, leading to densities close to Uranus. We also show that our method allows the derivation of mass ratios using only the 80 d of observations during the first campaign of K2.

Key words: techniques: photometric – techniques: radial velocities – time – planets and satellites: detection – planets and satellites: dynamical evolution and stability – planets and satellites: individual: EPIC201505350, K2-19.

1 INTRODUCTION

Transit timing variations (TTVs) are caused by the mutual gravitational interaction of planets which perturb each others' orbit. These are larger when the planets are close to mean-motion resonances (MMRs; Miralda-Escudé 2002; Agol et al. 2005; Holman & Murray 2005). Therefore, most of the known TTV systems are close

to MMRs. For example, the first detected system showing TTVs, Kepler-9 (Holman et al. 2010), is a system composed of a pair of transiting Saturn-mass planets near the 2:1 MMR and an inner earth-sized companion. However, the high precision and long baseline of *Kepler* (Borucki et al. 2010) also made it possible to detect TTVs in systems away from resonance (Almenara et al. 2015; Bruno et al. 2015).

In near-resonant systems the resonant angles which measure the displacement of the longitude of the conjunction from the periapsis of each planet, circulate (or librate) over a period much longer than

the orbital period of the outer planet, called the libration period or superperiod. Lithwick, Xie & Wu (2012) showed that for systems close to first-order MMRs the TTV signal is sinusoidal and that this libration period is inversely proportional to the distance to the resonance. Furthermore, the TTV amplitude depends on planet mass and hence TTVs provide another method to estimate planetary masses. However, since the TTV amplitude also depends on the free eccentricity, the TTV inversion problem is degenerate (Lithwick et al. 2012) unless the TTV curves are known with high accuracy as in the case of Kepler-9 (Holman et al. 2010; Borsato et al. 2014; Dreizler & Ofir 2014; Deck & Agol 2015).

Besides the resonant long-term periodicity, TTVs show a short-time-scale component 'chopping' which is related to the closest approach of both planets when the mutual gravitation interaction is strongest and occurs in the synodic time-scale (Nesvorný & Beaugé 2010; Nesvorný & Vokrouhlický 2014; Deck & Agol 2015). The chopping component of the TTVs is smaller than the resonant term and hence more difficult to detect. Recently, Nesvorný & Vokrouhlický (2014) and Deck & Agol (2015) showed that for low eccentricity, nearly co-planar systems the synodic chopping term depends only on the mass ratios and not on the eccentricity and hence makes it possible to uniquely estimate the planetary masses. The detection of the chopping component of the TTVs allowed the determination of unique solutions for a few systems e.g. KOI-872 and KOI-142 (Nesvorný et al. 2012, 2013).

Dynamic analyses of TTVs in *Kepler* transiting multiplanetary systems have allowed a better characterization of the system and/or helped confirm the planetary nature of many candidates. In particular, *Kepler* data has shown a pile-up of planet pairs wide but close to first-order MMRs and a gap narrow of these resonances (Lissauer et al. 2011; Fabrycky et al. 2014). This could be due to dissipation leading to 'resonant repulsion' (Lithwick & Wu 2012; Batygin & Morbidelli 2013).

After the failure of two out of four of the reaction wheels of the *Kepler* satellite the pointing accuracy was severely degraded. Cleaver engineering allowed the continuation of the mission in a new configuration named K2 (Howell et al. 2014). K2 observes four fields a year close to the Ecliptic. The short duration of the observations of each field (∼80 d) does not favour the detection of TTVs amongst planetary candidates discovered in these observations.

K2-19 (EPIC201505350) is a multiplanetary system detected in the K2 Campaign 1 (C1) data by Armstrong et al. (2015b). The K2 observations show two transiting planets one with an orbital period $P_b \sim 7.92$ d and radius $R_b = 7.23 \pm 0.60\,R_\oplus$ and a companion close to the 3:2 MMR with an orbital period $P_c \sim 11.91$ d and radius $R_b = 4.21 \pm 0.31\,R_\oplus$. The closeness to resonance implied that K2-19 was a good candidate for TTV and the brightness of the host star allowed follow-up transit observations from the ground. Approximately 200 d after the end of the K2 C1, a ground based transit was obtained showing TTVs of the inner planet with an amplitude of 1 h, allowing the authors to validate the system.

In this paper, we present a photodynamical analysis of the K2-19 system using K2 observations, three ground based transits of K2-19b and radial velocities (RVs) of the host star observed with the SOPHIE spectrograph. We show that although the libration period is not well constrained, we are able to characterize the system due to the detection of the short-period TTVs (chopping) in both companions. This was possible due to a photodynamical model that simultaneously fits the photometric transit observations, the RVs and the system dynamics. In Section 2, we describe the observations and in Section 3, we present the spectral characterization of the host star. We describe the photodynamic model in Section 4 and

present our results in Section 5. Finally, we discuss our results in Section 6.

2 OBSERVATIONS

2.1 K2 data

K2-19 was observed during Campaign 1 of the K2 mission between 2014 June 3 and August 20 spanning ∼80 d. We downloaded the pixel data from the Mikulski Archive for Space Telescopes (MAST)[1] and used a modified version of the *CoRoT* imagette pipeline (Barros et al. 2014) to extract the light curve. We computed an optimal aperture based on signal to noise of each pixel. The background was estimated using the 3σ clipped median of all the pixels in the image and removed before aperture photometry was performed. We also calculated the centroid using the Modified Moment Method by Stone (1989). For K2-19, we found that a 30 pixels photometric aperture resulted in the best photometric precision, this is roughly equivalent to an aperture radius of 3 pixels. A full description of the pipeline will be given in Barros et al. (in preparation).

The degraded pointing stability of the K2 mission couples with pixel sensitivity variations to introduce systematics in the raw light curves. Several methods to correct the systematics have been applied to the K2 data (Vanderburg & Johnson 2014; Aigrain et al. 2015; Armstrong et al. 2015a; Foreman-Mackey et al. 2015; Lund et al. 2015). In our case to correct for this flux dependence with position we used a procedure similar to Vanderburg & Johnson (2014). Due to the poor pointing accuracy, the targets slowly drift in the CCD and to correct for this, every 6 h the spacecraft thursters are fired returning the target to the initial position. Vanderburg & Johnson (2014) showed that the movement of the satellite was mainly in one direction. Thus, for each roll of the spacecraft, the target crosses a similar path in the CCD. This allows us to the use self-flat-fielding to correct the flux position variation by calculating the mean flux at each of a series of centroid position bins.

Following, Vanderburg & Johnson (2014), we start by estimating and removing stellar activity with a spline filter. Then we calculate the main direction of motion using principal component analysis. Finally, the flux dependence with position is computed and the correction is applied to the data. This 1D approximation starts failing after ∼10 d due to an extra slow drift of the satellite along the direction perpendicular to the main rolling motion. Hence, to maintain the 1D approximation, the light curves are divided in eight segments of equal duration and for each segment we performed the decorrelation method described above. After this self-flat-fielding procedure the spline filter is re-added to the light curve to avoid affecting the transits shape.

The final light curve of K2-19, with a mean rms of 840 ppm contains 10 transits of K2-19b and 7 of K2-19c. Three of the transits are simultaneous for the two planets. Noteworthy, the star shows rotational variability with a peak-to-peak amplitude of 1.5 per cent during the K2 observations. For the transit analysis we extracted individual transit light curves with length corresponding to three transit duration's and centred at the mid-transit time. Each transit was normalized by a quadratic baseline function. The K2 transit observations of both planets are shown in the top and middle panel of Fig. 1. We also show the median value of the distribution of models described in Section 4.

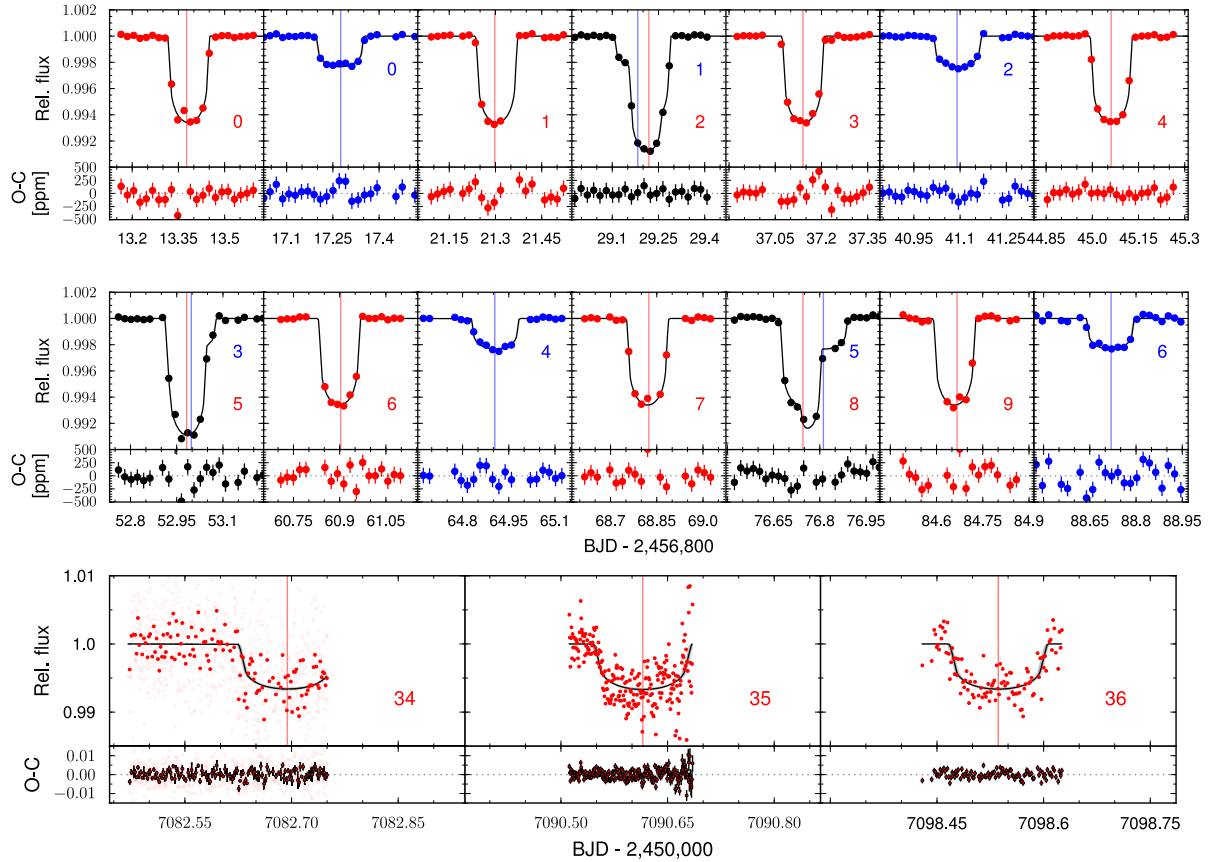[1] http://archive.stsci.edu/kepler/data_search/search.php

Figure 1. Transit observations of K2-19 in order of the transit time. For each transit, we overplotted the transit epoch and the transit time expected by a linear ephemeris (vertical lines). The black curve is the median value of the distribution of models (presented in Section 4) corresponding to 1000 random MCMC steps.

2.2 Ground based transits

The brightness of the host star (Kepmag = 12.8 mag) allows further observations from the ground. Hence, after the candidate detection we initiated a follow-up campaign. Three transits of K2-19b were observed from the ground 198 d after the K2 observations.

The first was observed on the 2015 February 28 by the 0.4-m Near Infrared Transiting ExoplanetS (NITES) telescope (McCormac et al. 2014, Fig. 1, bottom panel, epoch = 34). The telescope was defocused and a 20 s exposure time was used. Observations were performed with no filter. The data reduction was performed using standard IRAF[2] routines and DAOPHOT (Stetson 1987) to perform aperture photometry. This transit was already presented in Armstrong et al. (2015b).

The second transit was observed on 2015 March 8 at the 1-m C2PU/Omicron telescope in Calern (Observartoire de la Cote d'Azur). It is shown in the bottom panel of Fig. 1 (Epoch =35). The exposure time was 60 s and the Johnson-R filter was used. The data was reduced using the astro-ImageJ aperture photometry tool.

The third transit was observed on the 2015 March 16 at the Belesta 82-cm telescope (Fig. 1, bottom panel, epoch = 36). The exposure

time was 120 s and Johnson-R was used. The data was reduced with the ATV IDL tool (Barth 2001) which performs aperture photometry.

For each observation, differential photometry was performed using a careful selection of reference stars. The times were converted to Barycentric Dynamical Time using the IDL codes kindly made available by Eastman, Siverd & Gaudi (2010).

2.3 Spectroscopic observations

We obtained 10 spectroscopic observations of K2-19 from 2015 February 21 to April 25 with the SOPHIE spectrograph mounted on the 1.93 m telescope at the Observatoire de Haute-Provence (Perruchot et al. 2011; Bouchy et al. 2013). SOPHIE is a thermally stable high-resolution echelle optical spectrograph fed by a fibre link from the Cassegrain focus of the telescope. The fibre has a diameter of 3 arcsec on sky. The observations were obtained in the high-efficiency (HE) mode, which has a resolution R∼40 000 and covers a wavelength range of 390–687 nm.

The RVs were derived with the SOPHIE pipeline by computing the weighted cross-correlation function (CCF; Baranne et al. 1996; Pepe et al. 2002) with a G2 mask. The extracted Radial velocity (RVs) include corrections for charge transfer inefficiency of the SOPHIE CCD (Bouchy et al. 2009) using the procedure described in Santerne et al. (2012). The SOPHIE HE mode exhibits instrumental variations at long time-scales with an amplitude of a few m s⁻¹. These were corrected for using observations of a bright and stable

---

[2] IRAF is distributed by the National Optical Astronomy Observatories, which are operated by the Association of Universities for Research in Astronomy, Inc., under cooperative agreement with the National Science Foundation.

Table 1. Radial velocity measurements for K2-19 taken with SOPHIE.

BJD_{UTC} -2457000	RV (km s^{-1})	σ_{RV} (km s^{-1})	Vspan (km s^{-1})	σ_{Vspan} (km s^{-1})	FWHM	σ_{FWHM}	T_{exp} (s)	S/N/pix (550 nm)
046.64374	7.250	0.014	−0.057	0.036	10.406	0.034	2700	21.6
053.55195	7.203	0.023	−0.022	0.060	10.537	0.057	1800	19.2
054.72060	7.252	0.016	0.0002	0.041	10.601	0.039	2200	22.1
055.70836	7.229	0.033	−0.026	0.087	10.587	0.083	400	13.5
056.62866	7.219	0.025	−0.091	0.065	10.303	0.062	1573	16.7
075.65385	7.235	0.020	−0.013	0.055	10.265	0.049	3600	17.2
076.46383	7.200	0.019	−0.016	0.049	10.525	0.047	3600	18.7
079.53034	7.236	0.014	0.001	0.036	10.335	0.034	3600	26.8
109.59053	7.181	0.030	−0.102	0.076	10.366	0.073	3600	14.1
137.38239	7.209	0.028	−0.103	0.074	10.573	0.071	3066	14.5
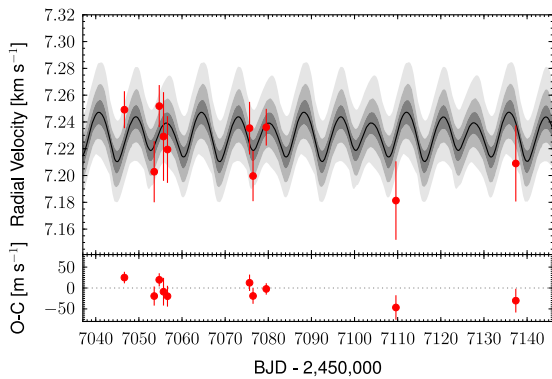
Figure 2. SOPHIE RVs as a function of time and the corresponding residuals. The overplotted black curve is the median value of the distribution of models (described in Section 4) corresponding to 1000 random MCMC steps, and the different shades of grey represent the 68.3, 95.5, and 99.7 per cent Bayesian confidence intervals.

star, HD 185144, obtained on the same nights and with the same instrument setup (Santerne et al. 2014). The bisector (Vspan) and full width at half-maximum errors have been estimated using the scaling relation published in Santerne et al. (2015).

The average signal-to-noise ratio of each spectra is 18 per pixel at 5500 Å and the average RV uncertainty is 22 m s^{-1}. The measurements and the respective uncertainties are given in Table 1. In the same table we also list the exposure time, signal-to-noise ratio per pixel at 550 nm and the bisector span of the CCF. The RV measurements are shown in Fig. 2 together with the model described in Section 4.

3 HOST STAR

We obtained the atmospheric parameters of the host star from the spectral analysis of 10 co-added SOPHIE spectra. First, we subtracted any sky contamination (using the spectra of fibre B) from the spectra pointing to the source (in fibre A) while correcting for the relative efficiency of the two fibres. The final spectrum has a S/N of ∼35 around 6070 Å.

To derive the atmospheric parameters, namely the effective temperature (T_{eff}), surface gravity (log g), metallicity ([Fe/H]), and microturbulence (ξ_t), we followed the methodology described in Tsantaki et al. (2013). This method relies on the measurement of the equivalent widths (EW) of Fe I/Fe II lines and by imposing excitation and ionization equilibrium. The analysis was performed in local thermodynamic equilibrium using a grid of model atmospheres (ATLAS9; Kurucz 1993) and the radiative transfer code MOOG

(Sneden 1973). Due to the low S/N of our spectrum, the EWs were derived manually using the IRAF splot task to avoid errors in the measurements.

From the above analysis, we obtain the following atmospheric parameters for the host star: $T_{eff} = 5390 \pm 180$ K, log $g = 4.42 \pm 0.34$ dex, $\xi_t = 1.02 \pm 0.24$ km s^{-1}, and [Fe/H] = 0.19 $\pm$ 0.12 dex, hence it is a K-dwarf. The spectroscopic gravity of the EW method is usually not well constrained when compared with other more model-independent methods such as from asteroseismology (Mortier et al. 2014) or from the parallax (Tsantaki et al. 2013; Bensby, Feltzing & Oey 2014). Therefore, we calculated the correction for the spectroscopic surface gravity using the calibration described in Mortier et al. (2014, equation 2) and found perfect agreement with our spectroscopic results (log g_{corr} = 4.42 dex). The derived parameters agree with the ones previously presented by Armstrong et al. (2015b). The larger number of spectra led to a lower uncertainty of the combined spectra which allowed a much better constraint on the derived stellar spectroscopic parameters. The uncertainty on these are approximately half of those found previously.

Using the above parameters for the host star T_{eff}, log g, and [Fe/H] we derive the stellar mass and radius by interpolating the stellar evolution models of Geneva (Mowlavi et al. 2012), Dartmouth (Dotter et al. 2008), and PARSEC (Bressan et al. 2012) using the MCMC described in Díaz et al. (2014). We obtained $M_* = 0.918^{+0.086}_{-0.070}$ M$_\odot$ and $R_* = 0.926^{+0.19}_{-0.069}$ R$_\odot$. These are also in agreement with the values presented by Armstrong et al. (2015b).

4 PHOTODYNAMICAL MODEL

All the transits and RVs were modelled simultaneously with an *n*-body dynamical integrator that accounts for the gravitational interactions between all components of the system. We use the MERCURY *n*-body integrator (Chambers 1999) to compute the three-dimensional position and velocity of all system components as a function of time. We assume that only the host star and two planets are present. The stellar velocity projected on to the line of sight is used to model the observed RVs. To model the transits, we use the Mandel & Agol (2002) transit model parametrized by the planet-to-star radius ratio, quadratic limb darkening coefficients for each filter and using the sky projection of the planet–star separation computed from the output of MERCURY. To account for the 29.4 min integration time, the transit model was oversampled by a factor of 20 and binned to the cadence of the data points. This photodynamical model is coupled to a Monte Carlo Markov Chain (MCMC) routine, described in detail in Díaz et al. (2014), in order to derive the posterior distribution of the parameters.

Table 2. Model parameters. Posterior mode and 68.3 per cent credible intervals. The orbital elements have the origin at the star (asteroidal parameters in the MERCURY code) and are given for the reference time $t_{\rm ref} = 2456813$ BJD.

Parameter	Mode and 68.3 per cent credible interval	
Stellar mass, $M_\star$ [M$_\odot$][a]	0.949 ± 0.077	
Stellar radius, $R_\star$ [R$_\odot$][a]	0.913 ± 0.094	
Stellar density, $\rho_\star$ [$\rho_\odot$]	1.25 ± 0.33	
Surface gravity, $\log g$ [cgs]	4.493 ± 0.085	
Systemic velocity, γ [km s^{-1}][a]	7.2296 ± 0.0080	
Linear limb darkening coefficient, u_a[a, c]	$0.460 \pm 0.026, 0.442 \pm 0.036, 0.476^{+0.027}_{-0.045}, 0.435^{+0.049}_{-0.023}$	
Quadratic limb darkening coefficient, u_b[a, c]	$0.210^{+0.019}_{-0.033}, 0.231^{+0.017}_{-0.029}, 0.232 \pm 0.026, 0.232 \pm 0.025$	
	Planet b	Planet c
Semimajor axis, a [au]	0.0762 ± 0.0022	0.1001 ± 0.0029
Eccentricity, e	$0.119^{+0.082}_{-0.035}$	$0.095^{+0.073}_{-0.035}$
Inclination, i [°][a]	$88.87^{+0.16}_{-0.60}$	$88.92^{+0.14b}_{-0.41}$
Argument of pericentre, ω [°]	179 ± 52	237^{+15}_{-68}
Longitude of the ascending node, n [°][a]	180 (fixed)	$173.1^{+2.9}_{-5.6}$
Mean anomaly, M [°]	253^{+61}_{-27}	110^{+54}_{-34}
Radius ratio, $R_p/R_\star$[a]	$0.07451^{+0.0014}_{-0.00045}$	$0.04515 \pm 7.3 \times 10^{-4}$
Planet mass, M_p [M$_\oplus$]	44 ± 12	$15.9^{+7.7}_{-2.8}$
Planet radius, R_p[R$_\oplus$]	7.46 ± 0.76	4.51 ± 0.47
Planet density, ρ_p [g cm^{-3}]	$0.492^{+0.26}_{-0.092}$	$0.94^{+0.46}_{-0.19}$
Planet surface gravity, $\log g_p$ [cgs]	$2.923^{+0.058}_{-0.17}$	$2.952^{+0.090}_{-0.15}$
α_1 [BJD-2450000][d, a]	$6813.38356 \pm 4.5 \times 10^{-4}$	6817.2732 ± 0.0013
α_2 [d][d, a]	$7.92008 \pm 4.0 \times 10^{-4}$	11.9068 ± 0.0013
SOPHIE jitter[a]	$1.15^{+0.47}_{-0.16}$	
Photometric jitter[a, c]	$1.016 \pm 0.052, 0.717 \pm 0.020, 1.429^{+0.094}_{-0.041}, 1.403^{+0.060}_{-0.12}$	
$q_+ = \frac{M_{p,b}+M_{p,c}}{M_\star}$[a]	$0.000198 \pm 4.7 \times 10^{-5}$	
$q_p = \frac{M_{p,c}}{M_{p,b}}$[a]	0.42 ± 0.12	
$e_c \cos \omega_c - \frac{a_b}{a_c} e_b \cos \omega_b$[a]	0.0146 ± 0.0043	
$e_c \cos \omega_c + \frac{a_b}{a_c} e_b \cos \omega_b$[a]	$-0.168^{+0.11}_{-0.070}$	
$e_c \sin \omega_c - \frac{a_b}{a_c} e_b \sin \omega_b$[a]	-0.067 ± 0.019	
$e_c \sin \omega_c + \frac{a_b}{a_c} e_b \sin \omega_b$[a]	$-0.02^{+0.11}_{-0.18}$	

Notes. [a]MCMC jump parameter.

[b]Reflected with respect to $i = 90°$, the supplementary angle is equally probable.

[c]Values for K2, NITES, C2PU, and Balesta, respectively, made to reduce the number of lines.

[d]$\alpha_1 \equiv t_{\rm ref} - \frac{\alpha_2}{2\pi} (M - E + e \sin E)$ with $E = 2 \arctan \left\{ \sqrt{\frac{1-e}{1+e}} \tan \left[\frac{1}{2} \left(\frac{\pi}{2} - \omega \right) \right] \right\}$; $\alpha_2 \equiv \sqrt{\frac{4\pi^2 a^3}{GM_\star}}$.

[e]M$_\odot = 1.98842 \times 10^{30}$ kg, R$_\odot = 6.95508 \times 10^8$ m, M$_\oplus = 5.9736 \times 10^{24}$ kg, R$_\oplus = 6.378137 \times 10^6$ m.

For each step of the MCMC a MERCURY run is performed using Bulirsch–Stoer algorithm with a 0.01 d time step for the photometry (that implies a maximum model related photometric error of 1ppm) and a 0.02 d time step for the RVs. The parameters of the system used in the fit are the stellar mass and radius, the limb darkening coefficients, the systemic velocity, the planetary masses, the planet-to-star radius ratio, and the planetary orbital parameters (orbital semimajor axis a, eccentricity e, orbital inclination i, argument of the periastron ω, longitude of the ascending node, n, and the mean anomaly M) at reference time $t_{\rm ref}$ which we choose to be 2456813 BJD. To minimize correlations between the model parameters which prevent adequate exploration of the parameter space, we used the Huber et al. (2013) parametrization (see Table 2). Furthermore, we fitted a normalization factor for each photometric data set and a multiplicative jitter parameter for the RVs and each photometric data set.

To define the reference plane we set the longitude of the ascending node of planet b to 180°. The system is symmetric relative to the inclination of one of the planets, hence we constrain the inclination of the planet b to one hemisphere ($i_b < 90°$) but allow the planet c to transit both hemispheres ($i_b < 180°$). As shown by Almenara et al. (2015), if the RV measurements and the transit photometry have high enough precision, our model completely constrains the system without requiring additional information about the host star. However, we performed test runs and concluded that the RV measurements are not precise enough to detect the stellar reflex velocity due to any of the planets. Moreover, the transit derived stellar density is not well constrained due to the poor sampling of the K2 observations and the precision of the ground-based transits. Therefore, to help constrain the system we included Gaussian priors on the stellar mass and radius derived from the spectroscopic observations. We also use Gaussian priors for the limb darkening coefficients based on the tables of Claret & Bloemen (2011). We use non-informative uniform priors for all the remaining model parameters. We run 46 independent MCMC chains and combined the results as described by Díaz et al. (2014) resulting in a final merged chain with 3500 independent points. Further details about the photodynamic method can be found in Almenara et al. (2015).
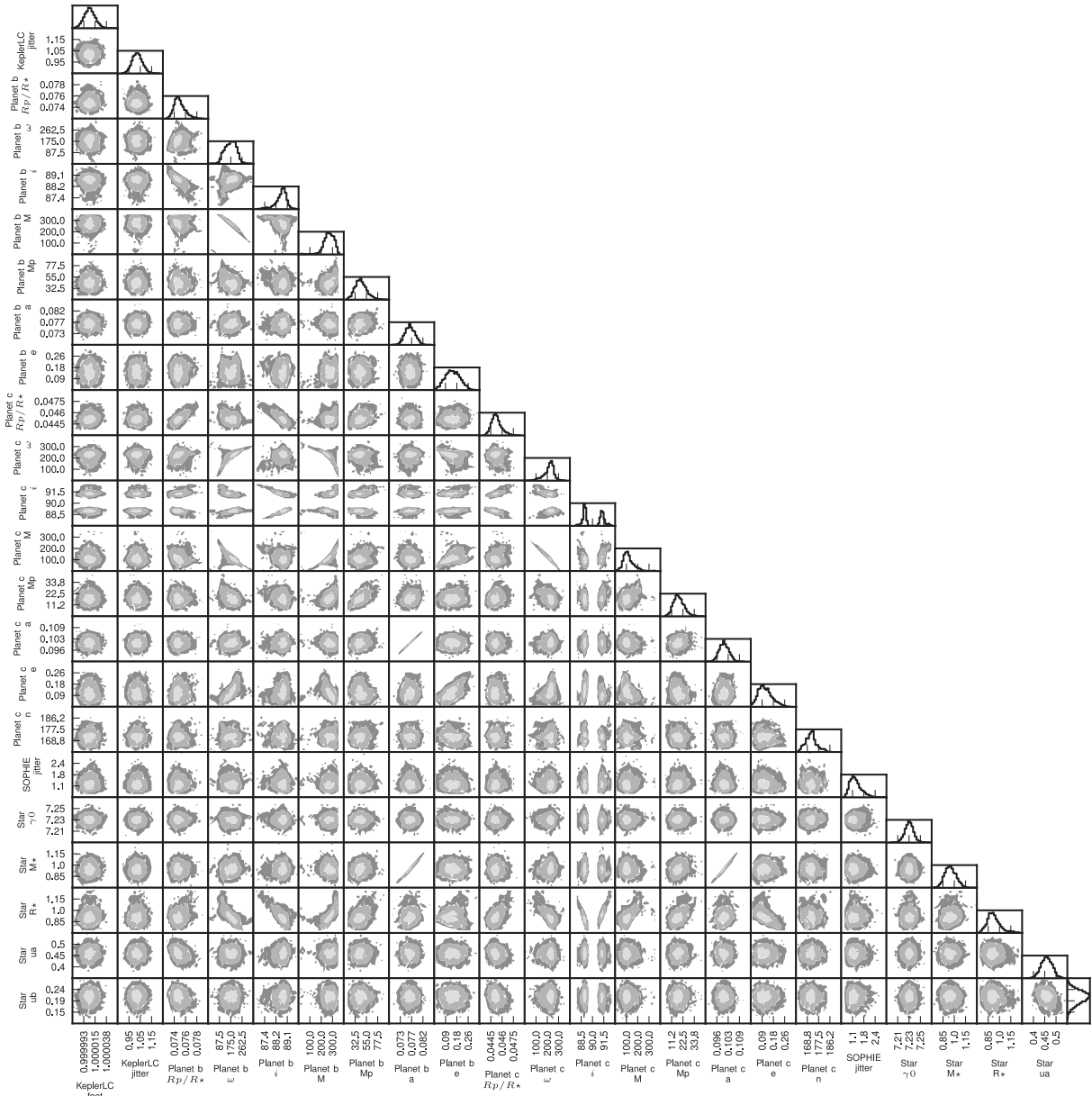
Figure 3. Correlation plots and posterior distribution of the fitted parameters of our model. We cannot distinguish which hemisphere planet c orbits as the two configurations are equally probable.

5 RESULTS

The mode and the 68.3 per cent confidence interval for the derived system parameters are given in Table 2. We find that K2-19b has a mass of 44 ± 12 M$_\oplus$ and radius of 7.46 ± 0.76 R$_\oplus$ and K2-19c has a mass of $15.9^{+7.7}_{-2.8}$ M$_\oplus$ and a radius of 4.51 ± 0.47 R$_\oplus$. The inclination of planet c could not be constrained to either hemisphere. For clarity, in Table 2 we give only the solution where planet c orbits the same hemisphere as planet b. However, both values of the inclination: $88.92^{+0.14}_{-0.41}$ and $91.19^{+0.41}_{0.14}$ are equally probable. The correlations between the parameters and the posterior parameter distributions are presented in Fig. 3.

As mentioned above, in our analysis we included stellar priors to scale the system. However, with only photometry and RVs it is possible to derive a solution independent of stellar models albeit with a poorer constrain on the scale of the system. We re-run the photodynamical model with uniform priors in stellar mass

and density and uniform priors in the linear limb darkening coefficients. As expected, this results in larger errors for the physical parameters that depend on the scale such as the stellar parameters: $R_\star = 0.73^{+0.98}_{-0.28}$ R$_\odot$ and $\rho_\star = 2.01^{+0.72}_{-0.24}$ $\rho_\odot$ which propagate to other physical parameters. Noteworthy is that the poorer constraint on the stellar density biases the orbital eccentricities to higher values $e_b = 0.309^{+0.055}_{-0.10}$ and $e_c = 0.271 \pm 0.072$ than the values derived when stellar priors are included (see Table 2). However, the mass ratios are determined by the system dynamics and hence are independent of the scale of the system. Therefore, they are well constrained and in agreement with the results obtained with the stellar priors $q_+ = \frac{M_{p,b} + M_{p,c}}{M_\star} = 0.000142^{+0.000038}_{-0.000023}$ and $q_P = \frac{M_{p,c}}{M_{p,b}}$ $= 0.474^{+0.16}_{-0.084}$. In case more precise stellar parameters are determined in the future, these mass ratios should be used to re-derive the planetary masses and the radius ratio to re-derive the planetary radius.
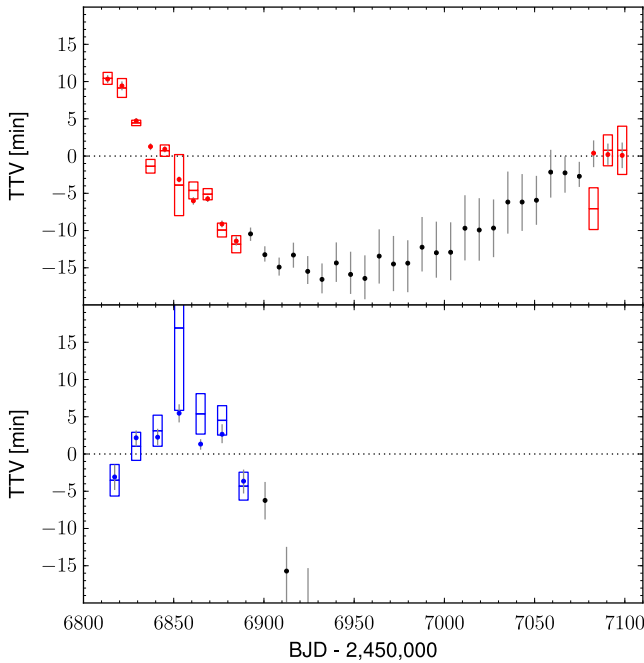
Figure 4. Comparison of the TTVs derived by the photodynamic model (as circles) with TTVs derived using a standard transit fitting (as boxes with the size of the 1σ error) for planet b (top panel), and planet c (bottom panel). For each planet, we use the respective ephemeris derived using the photodynamic estimated values of only the observed transits which are marked in red for planet b and in blue for planet c.

5.1 Transit times

To derive the transit times, we calculate the mid-point between the first and fourth transit contact using the MERCURY dynamic model output. Therefore, our transit time measurements include information on the system architecture and dynamics and as such are better constrained than direct measurement of the transit times in the light curve. However, we assume that only the host star and the two discussed planets are present in the system. For the case of Kepler-117, it was shown that the precision of the transit times with the photodynamic model is three times the precision of a direct fit of the transit times (Almenara et al. 2015).

For comparison, we computed the transit times directly from the K2 light curves using a procedure similar to what is described in Barros et al. (2013). For each planet the transits were fitted simultaneously ensuring the same transit shape. In Fig. 4, we compare the derived transit times using the photodynamic model and the transit times derived with a standard procedure. To compute the ephemeris we use only the values of the observed transit times derived with the photodynamic model. For planet b we derived the ephemeris: T_b (BJD) = 7.921101(69) × Epoch + 2456813.3767(21) and for planet c T_c (BJD) = 11.90727(58) × Epoch + 2456817.2755(22). For each planet the respective and same ephemeris was subtracted from the transit times derived with both methods so that we could directly compare them.

We find that the difference of the transits times for both methods is less than 3σ hence the transit times from both methods agree. The higher discrepancy is found for epochs 3 and 34 of planet b (the 4th and 35th data point in Fig. 4). The transit at epoch 3 shows signs of systematic noise and the transit at epoch 34 is incomplete. It has been shown by Barros et al. (2013) that, in these cases, the errors

of the transit times are underestimated, therefore, a difference of 3σ is not surprising. Noteworthy, when analysing the results of the traditional method we find that a linear ephemeris can be rejected at ∼100 per cent and ∼99.9 per cent, respectively, for planet b and planet c. Moreover, for both planets, the periodogram of the transit times shows a peak at the synodic period of the system, albeit not significant.

Using our photodynamic method, we obtain the double of the precision of the transit times as compared to the traditional method that does not include the dynamical constrains. For the K2-19 system the difference increases the significance of the TTVs for planet b and planet c, even in the short duration of the K2 observations, allowing us to better constraint the system architecture. Furthermore, the dynamical constrain reduces the impact of individual transits both with poor normalization or stellar activity, as long as enough transits are observed. This is because as shown by Deck & Agol (2015), TTVs may contain redundant information on the planetary masses. On the other hand, the TTVs derived with the photodynamic model are not pure measurements and depend on the validity of the model assumptions. For example, the existence of other planets in the system that could perturb the observed TTV has to be tested by comparing the photodynamic model derived TTVs with those derived directly from the light curve, as we did.

Armstrong et al. (2015b) predicted that the resonant time-scale of the system is ∼5 yr and hence it is not detectable with the current observation baseline. However, as mentioned above, the TTVs can show a chopping signal at the much shorter synodic time-scale. This chopping is clearly visible in Fig. 4, every three orbits of planet b it has a close encounter with planet c that changes its orbit and the transit times. This was also seen in KOI-884 system (Nesvorný & Vokrouhlický 2014; Nesvorný et al. 2014). In the same figure the chopping is also seen for K2-19c. Probably the closest encounter of both planets happens near the transit time since planet c and planet b show simultaneous transits during the K2 observations.

In our case the detection of the chopping signal at the short synodic time-scale allows us to directly determine planetary masses. This can be intuitively understood using the equations derived by Nesvorný & Vokrouhlický (2014) and Deck & Agol (2015) although our system might not obey their model assumptions. However, as expected, without the detection of the libration period the orbital eccentricities are poorly constrained. To better constrain the libration period of the system follow-up transits are very important and we encourage further follow-up in the next months to years. To illustrate our uncertainty in the libration period and estimate an ephemeris for the system we evolved 1000 random steps of our MCMC chain till the end of 2015. In Fig. 5, we show the model predicted TTVs with the 1σ uncertainty derived from the assembly of models. It is clear that we cannot predict the transit times with good accuracy further than 200 d into the future. This is because of the uncertainty in the system parameters and the fact that we do not sample the full libration cycle. Noteworthy is the different shape of the TTVs of K2-19c in Figs 4 and 5. This is due to the different ephemeris (especially the mean period) used to calculate the TTVs. In each case the ephemeris was calculated from different sets of transits times, for Fig. 4 we use only the observed transits while for Fig. 5 we used all the times presented in that figure. Since the duration of the observations for K2 is too short to sample the resonant time-scale, the period measured from K2 observations can be significantly different from the mean period of the system which can only be observationally probed with a much longer time span of the observation.
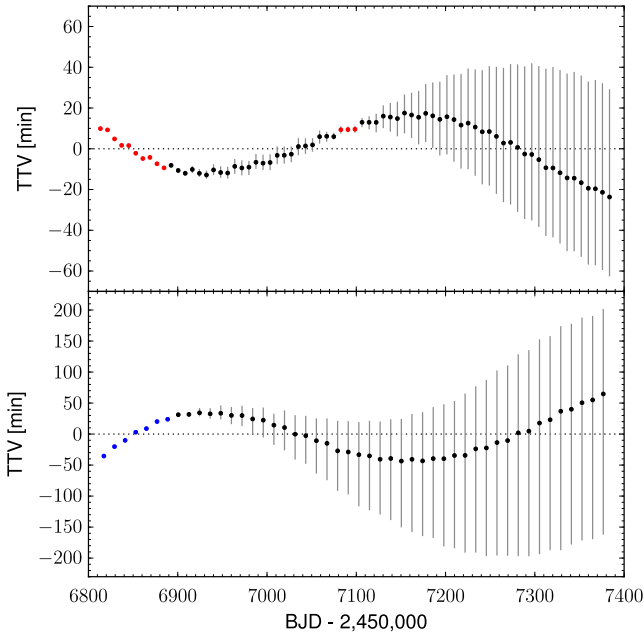
Figure 5. Prediction of the TTVs according to the photodynamic model until the end of 2015 for planet b (top panel) and planet c (bottom panel). For each planet, we use the respective ephemeris derived from the points plotted. For K2-19b the chopping signal is also visible in this figure. Three transits are nearly on a linear ephemeris and there is an offset from the next three transits due to the conjunctions with the outer planet.

We found no transit duration variations for the observed transits. Interestingly, the difference on the ascending node of both planets is $6.9^{+2.9}_{-5.6}$, if this is found to be significant it implies orbit precession that leads to a variation of the transit duration. We estimate that by the end of 2017 the transit duration of planet b will increase by 0.23 ± 0.12 h. For planet c, we expect a higher change but with higher uncertainty. Further high precision transits are needed to probe the long-term evolution of the system and help constrain the system parameters.

5.2 Model tests

Transit time measurements can be affected by red noise in the light curve (Barros et al. 2013). These spurious TTVs could lead to an overfitting of the model and a trapping of the solution. To test this hypothesis we multiplied the errors of the K2 transit light curves by three and repeated the analysis. We find that the errors of the measured transit times increase by a factor of 2–3 but the model is still constrained and we obtain system parameters within 1σ of the previous results although with uncertainties that are up to 50 per cent higher.

To further test our model, we use the photodynamic model described above fitting only the K2 light curve and using neither RV nor ground-based transits nor stellar priors. As expected, the derived parameter distributions are wider, however we still find the best solution in agreement with the previous results. In particular the mass ratios are very well constrained $q_+ = 0.000159^{+0.000075}_{-0.000018}$ and $q_p = 0.481^{+0.24}_{-0.076}$. Because we do not include stellar priors, the scale is not constrained. While stellar density is somewhat constrained by the transits $\rho_\star = 2.04^{+1.7}_{-0.49}\,\rho_\odot$, the stellar radius is unconstrained by the observations and its posterior distribution has the shape of the uniform prior.
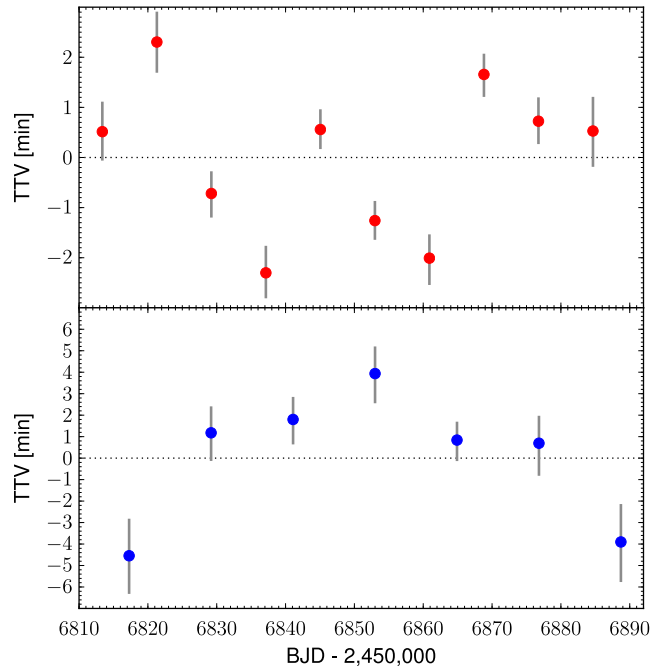
Figure 6. Transit times derived from K2 observations with the photodynamic model after removing a linear ephemeris for planet b (top panel), and planet c (bottom panel).

This test using only the K2 light curve predicts the times of the follow-up ground-based transits to be $2457082.65858^{+0.076}_{-0.094}$, $2457090.57608^{+0.082}_{-0.10}$, $2457098.49117^{+0.09}_{-0.11}$, respectively, for epochs 34, 35, and 36 which are within 1σ of the measured values. Therefore, we conclude that our system solution is robust and it is not significantly affected by spurious TTV due to systematics or spots. The TTVs derived using only the K2 observations are shown in Fig. 6 where the chopping is clearly visible. So this method will be useful for short duration observations like K2, Transiting exoplanet survey satellite (TESS) and Characterising exoplanet satellite (CHEOPS).

6 DISCUSSION

We present a photodynamic analysis of the K2-19 system discovered in the C1 campaign of K2. This system is composed of a slightly metal-rich K dwarf with $M_* = 0.949 \pm 0.077\,\mathrm{M_\odot}$ and $R_* = 0.913 \pm 0.094\,\mathrm{R_\odot}$ and two transiting planets very close to 3:2 MMR. K2-19b has a mass, $M_b = 44 \pm 12\,\mathrm{M_\oplus}$, a radius $R_b = 7.46 \pm 0.76\,\mathrm{R_\oplus}$ and an orbital period $P_b \sim 7.92\,\mathrm{d}$ and K2-19c has a mass, $M_c = 15.9^{+7.7}_{-2.8}\,\mathrm{M_\oplus}$, a radius $R_c = 4.51 \pm 0.47\,\mathrm{R_\oplus}$ and an orbital period, $P_c \sim 11.91\,\mathrm{d}$. K2-19c is similar to Uranus. The radius derived for both planets is in agreement with those derived previously by Armstrong et al. (2015b). However, our analysis allow a much better constraint on the mass of the planets. In Fig. 7, we show the position of K2-19b and K2-19c in the mass–radius diagram compared with known planets with M < 50 $\mathrm{M_\oplus}$ and R < 10 $\mathrm{R_\oplus}$. In the same figure, we plot the theoretical models for solid planets with a composition of pure iron and pure water (Zeng & Sasselov 2013). We also plot the models of Baraffe, Chabrier & Barman (2008) which apply to planets with gaseous envelopes and different heavy material enrichments assuming and an age of 5 Gyr. Clearly, K2-19b and K2-19c are less dense than a pure water/ice sphere, therefore they have a significant gas envelope. K2-19c probably has
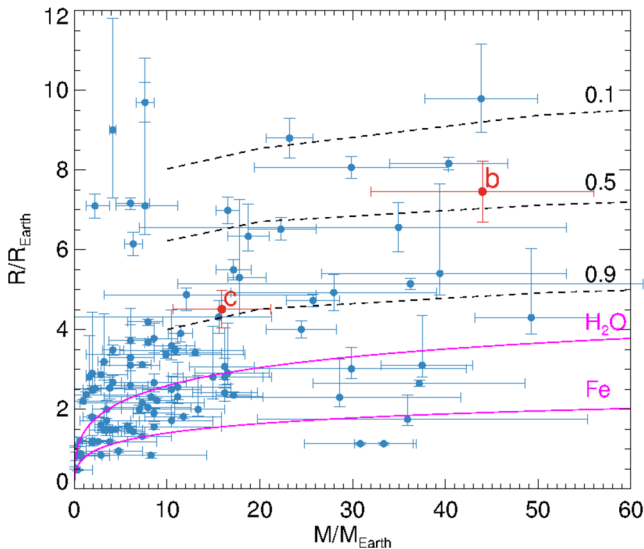
Figure 7. Mass–radius relationship for different bulk composition of planets. In magenta solid lines we show the models of Zeng & Sasselov (2013) for solid planets with a composition of pure iron and pure water. In black dashed lines we show the models of Baraffe et al. (2008) for gaseous planets with heavy material enrichments of $Z = 0.1$, 0.5, and 0.9 assuming and an age of 5 Gyr. We superimposed the known planets in this mass–radius range and the position of the planet K2-19b and K2-19c marked with a respective red letter.

a high fraction of heavy elements and hence, a core while K2-19b probably has less heavy elements which results in a lower density.

We present follow-up transit photometry and spectroscopic observations that together with the K2 observations allow us to uniquely characterize the system. We also show that even using only the K2 photometry, we can derived the mass ratios of the system and find the same unique solution. This is due to the detection of the chopping short time-scale TTVs in both planets produced by the orbital conjunctions between the planets. In our case the non-detection of the full libration curve leads to a poor constraint on the orbital eccentricity but does not prevent finding a unique solution. We predict a libration period of ∼1.5 yr but further observations are needed to confirm it. We thus encourage further follow-up observations to sample the full TTV curve and derive the eccentricity. This will give further insight into the evolution and formation of this system (Kley & Nelson 2012), which is specially interesting since it is one of the closest systems to the 3:2 MMR known.

The predicted RV amplitude for planet b is 14.4 ± 4.2 m s^{-1} and for planet c is $4.9^{+2.0}_{-1.0}$ m s^{-1}, below the precision of SOPHIE for this target. However, they can be measured with any of the HARPS instruments since the target is visible from both the Canary Islands and La Silla. Comparing the TTV predicted mass with the one measured by RVs will be important to validate the TTV mass determination method and probe the existence of additional companions. Weiss & Marcy (2014) state that amongst their sample of 65 exoplanets smaller than 4 Earth radii, the masses determined by TTVs are statistically lower than masses estimated by RVs. An example of this discrepancy is KOI-94-d (Borucki et al. 2011) whose mass is $106 \pm 11 M_\oplus$ (Weiss et al. 2013) according to the RV analysis, whereas the TTV analysis gives $52.1 \pm 7\ M_\oplus$ (Masuda et al. 2013). However, for KOI-142b (Kepler-88b) the TTV derived masses are in agreement with the RVs derived masses (Nesvorný et al. 2013; Barros et al. 2014). Understanding the discrepancies is very important to allow direct comparison between the TTV and RV estimated

masses. Furthermore, if the reflex motion of the star is measured it is possible to derive masses and radius for the system bodies without using stellar models (Almenara et al. 2015).

In traditional TTVs analysis of multiplanetary systems, the individual TTVs are first derived from transit fitting and later modelled using *n*-body dynamic simulations to constrain planetary masses. We show that fitting simultaneously the transit light curves with the system dynamics (photodynamical model) increases the precision of the TTV measurements and helps constrain the system architecture. Without this increase in precision we would not detect short period TTVs (chopping) and the mass ratios would be very poorly constrained (Armstrong et al. 2015b). Our method is a powerful tool for the analysis of the short duration K2 data and future observations with CHEOPS and TESS. Applying a photodynamic model will help characterize a higher number of systems and will lead to better understanding of the evolution of near-resonant systems.

REFERENCES

Agol E., Steffen J., Sari R., Clarkson W., 2005, MNRAS, 359, 567
Aigrain S., Hodgkin S. T., Irwin M. J., Lewis J. R., Roberts S. J., 2015, MNRAS, 447, 2880
Almenara J. M., Díaz R., Mardling R., Barros S. C. C., Damiani C., Bruno G., Bonfils X., Deleuil M., 2015, MNRAS, 453, 2644
Armstrong D. J. et al., 2015a, A&A, 579, A19
Armstrong D. J. et al., 2015b, preprint, A&A, 582, A33
Baraffe I., Chabrier G., Barman T., 2008, A&A, 482, 315
Baranne A. et al., 1996, A&AS, 119, 373
Barros S. C. C., Boué G., Gibson N. P., Pollacco D. L., Santerne A., Keenan F. P., Skillen I., Street R. A., 2013, MNRAS, 430, 3032
Barros S. C. C. et al., 2014, A&A, 569, A74
Barth A. J., 2001, in Harnden F. R., Jr, Primini F. A., Payne H. E., eds, ASP Conf. Ser. Vol. 238, Astronomical Data Analysis Software and Systems X. Astron. Soc. Pac., San Francisco, p. 385
Batygin K., Morbidelli A., 2013, AJ, 145, 1
Bensby T., Feltzing S., Oey M. S., 2014, A&A, 562, A71
Borsato L., Marzari F., Nascimbeni V., Piotto G., Granata V., Bedin L. R., Malavolta L., 2014, A&A, 571, A38
Borucki W. J. et al., 2010, Science, 327, 977
Borucki W. J. et al., 2011, ApJ, 728, 117
Bouchy F. et al., 2009, A&A, 505, 853
Bouchy F., Díaz R. F., Hébrard G., Arnold L., Boisse I., Delfosse X., Perruchot S., Santerne A., 2013, A&A, 549, A49
Bressan A., Marigo P., Girardi L., Salasnich B., Dal Cero C., Rubele S., Nanni A., 2012, MNRAS, 427, 127
Bruno G. et al., 2015, A&A, 573, A124
Chambers J. E., 1999, MNRAS, 304, 793

Claret A., Bloemen S., 2011, A&A, 529, A75
Deck K. M., Agol E., 2015, ApJ, 802, 116
Díaz R. F., Almenara J. M., Santerne A., Moutou C., Lethuillier A., Deleuil M., 2014, MNRAS, 441, 983
Dotter A., Chaboyer B., Jevremović D., Kostov V., Baron E., Ferguson J. W., 2008, ApJS, 178, 89
Dreizler S., Ofir A., 2014, preprint (arXiv:1403.1372)
Eastman J., Siverd R., Gaudi B. S., 2010, PASP, 122, 935
Fabrycky D. C. et al., 2014, ApJ, 790, 146
Foreman-Mackey D., Montet B. T., Hogg D. W., Morton T. D., Wang D., Schölkopf B., 2015, ApJ, 806, 215
Holman M. J., Murray N. W., 2005, Science, 307, 1288
Holman M. J. et al., 2010, Science, 1195778
Howell S. B. et al., 2014, PASP, 126, 398
Huber D. et al., 2013, Science, 342, 331
Kley W., Nelson R. P., 2012, ARA&A, 50, 211
Kurucz R., 1993, Kurucz CD-ROM No. 13, ATLAS9 Stellar Atmosphere Programs and 2 km/s grid. Smithsonian Astrophysical Observatory, Cambridge, p. 13
Lissauer J. J. et al., 2011, Nature, 470, 53
Lithwick Y., Wu Y., 2012, ApJ, 756, L11
Lithwick Y., Xie J., Wu Y., 2012, ApJ, 761, 122
Lund M. N., Handberg R., Davies G. R., Chaplin W. J., Jones C. D., 2015, ApJ, 806, 30
McCormac J., Skillen I., Pollacco D., Faedi F., Ramsay G., Dhillon V. S., Todd I., Gonzalez A., 2014, MNRAS, 438, 3383
Mandel K., Agol E., 2002, ApJ, 580, L171
Masuda K., Hirano T., Taruya A., Nagasawa M., Suto Y., 2013, ApJ, 778, 185
Miralda-Escudé J., 2002, ApJ, 564, 1019
Mortier A., Sousa S. G., Adibekyan V. Z., Brandão I. M., Santos N. C., 2014, A&A, 572, A95

Mowlavi N., Eggenberger P., Meynet G., Ekström S., Georgy C., Maeder A., Charbonnel C., Eyer L., 2012, A&A, 541, A41
Nesvorný D., Beaugé C., 2010, ApJ, 709, L44
Nesvorný D., Vokrouhlický D., 2014, ApJ, 790, 58
Nesvorný D., Kipping D. M., Buchhave L. A., Bakos G. Á., Hartman J., Schmitt A. R., 2012, Science, 336, 1133
Nesvorný D., Kipping D., Terrell D., Hartman J., Bakos G. Á., Buchhave L. A., 2013, ApJ, 777, 3
Nesvorný D., Kipping D., Terrell D., Feroz F., 2014, ApJ, 790, 31
Pepe F., Mayor M., Galland F., Naef D., Queloz D., Santos N. C., Udry S., Burnet M., 2002, A&A, 388, 632
Perruchot S. et al., 2011, in Shaklan S., ed., Proc. SPIE Conf. Ser. Vol. 8151, Techniques and Instrumentation for Detection of Exoplanets V. SPIE, Bellingham, p. 815115
Santerne A. et al., 2012, A&A, 545, A76
Santerne A. et al., 2014, A&A, 571, A37
Santerne A. et al., 2015, MNRAS, 451, 2337
Sneden C. A., 1973, PhD thesis, Univ. Texas
Stetson P. B., 1987, PASP, 99, 191
Stone R. C., 1989, AJ, 97, 1227
Tsantaki M., Sousa S. G., Adibekyan V. Z., Santos N. C., Mortier A., Israelian G., 2013, A&A, 555, A150
Vanderburg A., Johnson J. A., 2014, PASP, 126, 948
Weiss L. M., Marcy G. W., 2014, ApJ, 783, L6
Weiss L. M. et al., 2013, ApJ, 768, 14
Zeng L., Sasselov D., 2013, PASP, 125, 227

This paper has been typeset from a TEX/LATEX file prepared by the author.